APS physics

CHORUS

This is the accepted manuscript made available via CHORUS. The article has been published as:

Structural coherence and ferroelectric order in nanosized multiferroic YMnO_{3}

S. Tripathi, V. Petkov, S. M. Selbach, K. Bergum, M.-A. Einarsrud, T. Grande, and Y. Ren

Phys. Rev. B **86**, 094101 — Published 4 September 2012

DOI: 10.1103/PhysRevB.86.094101

Structural coherence and ferroelectric order in nanosized multiferroic $YMnO_3$

S. Tripathi[1], V. Petkov[1,*], S. M. Selbach[2], K. Bergum[2], M.-A. Einarsrud[2], T. Grande[2], and Y. Ren[3]

[1]Department of Physics, Central Michigan University, Mt. Pleasant, Michigan 48859, USA
[2]Department of Materials Science and Engineering, Norwegian University of Science and Technology, 7491 Trondheim, Norway
[3]Advanced Photon Source, Argonne National Laboratory, Argonne, Illinois 60439, USA

PACS: 64.70.Nd, 61.05.cp

e-mail: petkov@phy.cmich.edu

Abstract

Atomic-scale structure studies involving synchrotron x-ray diffraction (SXRD) and pair distribution function (PDF) analysis on a series of $YMnO_3$ particles with sizes ranging from 467±42 (bulk) to 10±1 nm are presented. Studies reveal that while the nanoparticles retain most of the characteristics of the layered hexagonal-type structure of the bulk, substantial local atomic displacements arise with diminishing particles size. The displacements lead to a very substantial loss of structural coherence in the particles of size smaller than 100 nm. The displacements mostly affect the Yttrium (Y) atoms and to a lesser extent the Mn-O sublattice in $YMnO_3$. We argue that the increased displacement of Y atoms along the polar c-axis of the hexagonal unit cell may result in enhanced local ferroelectric distortions with decreasing particles size. The planar, i.e. a- and b-axis direction displacements of Y atoms, however, may interfere with the cooperative ferroelectricity of nanosized $YMnO_3$, so future efforts to employ $YMnO_3$ in nanoscale applications should take them into account.

1. Introduction

Multiferroics have attracted considerable attention due to the coexistence of cooperative magnetic and ferroelectric properties that can be employed for several useful applications [1-3]. The understanding of the structural origin of these properties is of prime importance from both scientific and technological perspectives. Hexagonal $YMnO_3$ is an archetypal multiferroic material that exhibits spontaneous polarization below the ferroelectric transition temperature of $Tc_{FE} \approx 930$ K [4] and, antiferromagnetic ordering below the Neel temperature of $T_N \approx 70$ K [5]. Recent studies have shown a clear evidence of coupling between the ferroelectric and magnetic ordering in $YMnO_3$ [6]. At room temperature $YMnO_3$ is ferroelectric with a layered-type hexagonal structure (Space group $P6_3cm$: a_{Hex} = 6.155 Å, c_{Hex} = 11.403 Å; see Fig. 1) [7, 8]. The volume of the ferroelectric unit cell is three times larger than that of the unit cell of the high temperature paraelectric phase (S.G. $P6_3/mmc$: a', c') where $a_{Hex} = \sqrt{3}\, a'$ and $c_{Hex} = c'$ [8]. The ferroelectric phase is related to the paralectric phase by an antiferrodistortive ($Mn\text{-}O_5$ polyhedra tilt) transition leading to a cell tripling at the transition temperature $Tc_{AFD} \approx$ 1270 K [4], though this is not the ferroelectric transition temperature $Tc_{FE,}$ which is somewhat lower than Tc_{AFD} [1]. The antiferrodistortive and ferroelectric phase transitions in $YMnO_3$ are driven by simultaneous freezing of zone boundary (K_3 : q = 0 0 1/3) and zone center (Γ_1 : q = 0 0 0) phonon modes, respectively [1]. The ferroelectric phase of $YMnO_3$ is characterized by buckling of the MnO_5 polyhedra, accompanied by static displacements of the Y^{3+} ions along the c-axis of the hexagonal unit cell (see Fig. 1) leading to a net electric polarization. In perovskites of the ABO_3 family typically the ferroelectric order originates from hybridization between the empty B-site *3d* orbitals and empty O *2p* orbitals accompanied by off-centre displacements of the B ions. This "d^0-ness" criterion for ferroelectricity is not applicable to $YMnO_3$ due to the d-orbital occupation of the $Mn^{3+}(3d^4)$ magnetic ions [9].

The driving force for ferroelectricity in such "improper" ferroelectric hexagonal manganites has been a subject of debate for more than a decade. Early first principles electronic structure calculations discussed the possibility of "directional d^0-ness" of d^4 Mn^{3+} due to the crystal field splitting [10], but subsequent studies found no off-centering of Mn in the MnO_5 bipyramidal polyhedra [1]. Although hybridization between O 2*p*

orbitals and formally empty Y 4*d* orbitals has been found [11], a recent theoretical study of the chemical bonding shows that a covalency between oxygen and rare earth ions (Y) favours *centrosymmetry* rather than ferroelectricity in hexagonal manganites [12]. In contrast with ferroelectric perovskites, the driving force for polarization in hexagonal manganites is electrostatic, hence the term "geometric ferroelectrics" [1].

Currently technology is moving fast toward producing nanosized ferroelectric materials. The success of this effort requires a sound understanding of the ferroelectric phenomena at the nanoscale. Atoms in nanosized materials often may form structures different from the respective bulk leading to drastically modified physical properties [13-17]. Several studies like classical, phenomenological thermodynamic theory (Landau-Ginzberg-Devonshire approach) have predicted a phase transition from a ferroelectric to a paraelectric phase at a critical particle size of the order of a few tens of nanometers in nanosized ABO_3 ceramics [18-20] of the perovskites family. Experimental studies, however, have shown that the atomic displacements causing ferroelectricity in ABO_3 systems survive at the nanoscale [13]. Though, due to the presence of nanoscale structural disorder, the cooperative ferroelectricity is weakened very significantly. In a recent report Han et al [6] have shown that the cooperative magnetic order in $YMnO_3$ survives even in 25 nm particles with a small shift in the magnetic transition temperature. No comment on the cooperative ferroelectric order has been made so far for nanosized layered (i.e. non-perovskites type) materials such as $YMnO_3$. In this paper we report results from structure studies involving high-energy synchrotron radiation x-ray diffraction (SXRD) and atomic pair distribution function (PDF) analysis on a series of $YMnO_3$ particles with sizes ranging from 467±42 (bulk) to 10±1 nm aiming at revealing the evolution of the structural origin of ferroelectricity, i.e. the static displacements of Y atoms, with particles size. In particular, atomic PDFs studies have proven to be very efficient in determining the atomic scale structure of nanosized particles [14, 15, 21]. The results from the PDF analysis are compared with traditional Rietveld analysis of the SXRD data. We find that Yttrium (Y) atoms in $YMnO_3$ exhibit extra local displacements with diminishing particles size similar to what has been observed with Bi atoms in nanosized ferroelectric $BiFeO_3$ [14]. The implications of these extra displacements on the ferroelectric properties of nanosized $YMnO_3$ are discussed as well.

2. Experimental:

2.1 Sample Synthesis

Nanocrystalline hexagonal $YMnO_3$ was prepared by an aqueous chemical synthesis route described in detail in reference [22]. The particles size was controlled by careful annealing in air between 800 and 1250 ºC. The average particles' sizes referred to in this paper were determined by Rietveld refinement using fundamental parameters for the peak shape obtained with the NIST LaB_6 standard. The refined particles' sizes and the narrow size distributions were independently confirmed by transmission electron microscopy [22]. The cation stoichiometry was controlled through thermogravimetric determination of the cation concentrations of the Y and Mn precursor solutions used in the synthesis to ensure a 1:1 ratio of Y and Mn [22]. The oxygen stoichiometry of $YMnO_3$ is determined by the thermal history, the temperature and partial pressure of oxygen at the synthesis conditions. Thermogravimetric measurements have shown that $YMnO_3$ is oxygen stoichiometric under the synthesis conditions used to prepare the materials investigated in the present work [23].

2.2 Synchrotron Radiation Diffraction Experiments

Synchrotron XRD experiments were carried out in ambient conditions at the 11-ID-C beamline at the Advanced Photon Source using x-rays with energy of 115.232 keV (λ=0.1076 Å) and a large-area detector. Synchrotron radiation x-rays were used for two reasons. Firstly, the higher flux of synchrotron radiation x-rays makes it possible to measure the rather diffuse diffraction patterns of smaller size $YMnO_3$ particles with a very good statistical accuracy. Secondly, the higher energy of synchrotron radiation x-rays makes it possible to reach higher wavevectors, Q, which is essential for the atomic PDF analysis [13, 14, 21]. With the present experiments diffraction data was collected to wave vectors as high as 30 $Å^{-1}$. Experimental SXRD patterns are shown in Figure 2.

2.3 Rietveld Refinements of the XRD patterns

Rietveld analysis allows testing and refining of structure models based on one of the 230 space groups against the Bragg peaks in XRD patterns. The Rietveld analysis was done with the help of the program "Fullprof" [24]. PseudoVoigt function was used to describe the Bragg peak profiles while the background scattering was approximated by a sixth order polynomial. Rietveld refinements of the SXRD data were carried out for the

$YMnO_3$ samples with average sizes of 38±2, 45±2, 49±2, 121±3, 171±6, and 467±42 (bulk) nm using a structure model based on the $P6_3cm$ space group that corresponds to the ambient temperature ferroelectric phase of bulk $YMnO_3$. Due to the large smearing of the Bragg peaks in the respective SXRD patterns (see Fig. 2), the samples with sizes smaller than 38nm were not possible to be subjected to reliable Rietveld refinements. The asymmetric unit of the ferroelectric hexagonal cell contains 7 atoms: Y1 2(a): 0, 0, 0.25+δz; Y2 4(b): 1/3, 2/3, 0.25+δz; Mn 6(c): 1/3+δx, 0, 0; O1 6(c): 1/3+ δx, 0, 1/6+δz; O2 6(c): 2/3+δx, 0, 1/3+ δz; O3 2(a): 0, 0, 1/2 + δz; O4: 1/3, 2/3, 0+ δz [8]. In the Rietveld analysis, the lattice parameters of the hexagonal unit cell, the background, peak broadening parameters, peak profile shape function, the atomic coordinates and atomic isotropic thermal parameters were refined. The thermal parameters for O_3 and O_4 for particles of sizes smaller than 121 nm were fixed as they refined to unreasonably large values.

2.4 Pair Distribution Function analysis

Materials where the length of structural coherence is limited to a few nm, as it is the case with the smaller size $YMnO_3$ particles, are difficult to analyze structurally by Rietveld analysis. The reason is that the respective XRD patterns (see Fig. 2) show a very strong diffuse scattering component. Atomic PDFs are much better suited for the task [13-15, 21]. In brief, the frequently used atomic PDF G(r) is defined as $G(r) = 4\pi r[\rho(r)-\rho_0]$ where $\rho(r)$ and ρ_0 are the local and average atomic number densities, respectively, and r is the radial distance. G(r) peaks at characteristic distances separating pairs of atoms and thus reflects the atomic-scale structure. The PDF G(r) is the Fourier transform of the experimentally observable total structure function, S(Q), i.e.,

$$G(r) = (2/\pi) \int_{Q=Q_{\min}}^{Q_{\max}} Q[S(Q)-1]\sin(Qr)dQ, \qquad (1)$$

where Q is the magnitude of the wave vector ($Q= 4\pi\mathrm{Sin}\theta/\lambda$), 2θ is the angle between the incoming and outgoing radiation beams, and λ is the wavelength of the radiation used. Note the structure function, S(Q), is related to only the coherent/elastic part of the scattered x-ray intensities, $I^{coh.}(Q)$, as follows:

$$S(Q) = 1 + \left[I^{coh.}(Q) - \sum c_i \left| f_i\ (Q) \right|^2 \right] / \left| \sum c_i f_i(Q) \right|^2, \qquad (2)$$

where c_i and $f_i(Q)$ are the atomic concentration and x-ray scattering factor, respectively, for the atomic species of type *i.* The great advantage of atomic PDFs in studying materials of a limited length of structural coherence is that the total scattering, including Bragg scattering as well as diffuse scattering, is taken into account. In this way both the average (i.e. atomic longer-range) structure, manifested in the Bragg-like peaks, and local structural distortions, manifested in the diffuse component of the diffraction pattern, are reflected in the PDF. Also, atomic PDFs do not imply any periodicity and can be used to test and refine structure models for materials showing any degree of structural coherence, including going beyond the constraints of the 230 Space Groups that are used for perfectly crystalline materials.

The test and refinement of structure models against atomic PDFs was done using the sprogram PDFgui [25]. Data from literature sources for the crystal structures of bulk $YMnO_3$ were used as starting values in the PDF fitting. The lattice parameters of the hexagonal unit cell, the atomic coordinates and atomic isotropic thermal parameters were refined as to minimize a goodness-of-fit indicator, R_w, defined as:

$$R_w = \left\{ \frac{\sum w_i (G_i^{\exp.} - G_i^{calc.})^2}{\sum w_i (G_i^{\exp.})^2} \right\}^{1/2}, \qquad (3)$$

where $G^{exp.}$ and $G^{calc.}$ are the experimental and calculated PDFs, respectively, and w_i are weighting factors reflecting the statistical quality of the individual data points. Here it may be added that the best possible agreement factors achieved with the PDF fits are usually in the range of 10-20 % as is the case with the present fits for bulk $YMnO_3$ and larger size nanoparticles for example (e.g. see Fig. 7 later on introduced in the text). Such R_w's appear somewhat high when compared to goodness-of-fit factors resulted from Rietveld refinements of XRD data in reciprocal space. This mostly reflects the fact that the atomic PDFs being fit take both the sharp, Bragg like features and the diffuse component of the XRD data into account while Rietveld fits consider only the former. The inherently higher absolute value of the goodness-of-fit factors in PDFs fits, however, does not affect their functional purpose as a residuals quantity that guides the refinement

of the parameters of the tested structure models and so allows differentiating between them.

3. Results and Discussion

The SXRD patterns for bulk $YMnO_3$ particles studied here (see Fig. 2) show two types of sharp Bragg peaks: peaks due to the main hexagonal (high symmetry: aristotype) cell and superlattice peaks. Superlattice Bragg peaks (marked with a broken line in Fig. 2) arise from the tilting of the MnO_5 polyhedra and the antiparallel displacements of Yttrium (Y) cations (see Fig. 1). A careful look at the evolution of the SXRD patterns as a function of the particle's size shows that all sharp Bragg peaks almost disappear for particles of size smaller than 38 nm. Instead an intense diffuse scattering-like component appears and grows with diminishing particles size. For that reason we performed Rietveld analysis only on the SXRD patterns of the particles with sizes of 38 nm and higher.

As an example Figure 3 shows the observed and Rietveld calculated SXRD patterns for particles with size of 38, 49, 171 and 467 nm. The excellent fits between the observed and calculated SXRD patterns for the larger size particles confirms that they possess the structure type and stoichiometry of the $YMnO_3$ ferroelectric phase. For particles smaller than 38 nm the Rietveld fits progressively get worse. The worsening is manifested in two ways: Firstly, the complete smearing out of the distinct superlattice reflection (102) cannot be reproduced by the Rietveld fits. Secondly, Rietveld analysis cannot account for the diffuse scattering and the increasing Bragg peak broadening observed with the smaller size $YMnO_3$ particles. The evolution of the cell volume ($V_H=a_H^2c_H(\sqrt{3}/2)$), as obtained from the Rietveld refinements, is shown in Fig. 4 (a). Cell volume, together with the atomic positions of Y atoms, are important structural parameters used since they can be used to assess the ferroelectric properties of $YMnO_3$ as shown below. As can be seen in Fig. 4 (a) the unit cell volume variation with particles size can be fit well with an exponentially increasing function. An exponential-like variation of nanomaterials' properties with varying particle size has been reported in several studies. Some of the reported properties showing exponential-like variation with size are: the cohesive energy versus the size of metals such as molybdenum (Mo) and tungsten (W); the activation energy of diffusion versus the size for iron (Fe) and copper (Cu); the vacancy forming energy versus the size of spherical gold particles (Au); the band gap, bulk modulus,

melting temperature and Raman photon frequency shift of CdS, CdSe and ZnS quatum dots; and the dielectric properties of nanosized $BaTiO_3$. This variation has been suggested as an universal behavior for several structure-related properties of nanosized systems [13a, 26, 27].

The ferroelectric phase of $YMnO_3$ (SG: $P6_3cm$) sets in by breaking the center of inversion symmetry of the high temperature (paraelectric) phase resulting in antiparallel displacements of Y ions (see Fig. 1) and associated buckling of the MnO_5 polyhedra (bipyramids), leading to a net electric polarization. As can be seen in Fig. 1, $YMnO_3$ can be considered as built of layers of MnO_5 bipyramids that are separated by layers of Y atoms. Ferroelectricity is due to off-center displacements of Y (positive charge) and oxygen (negative charge) atoms along the polar c axis, giving rise to spontaneous polarization along the z direction/c axis of the hexagonal unit cell. Local-spin-density approximations (LDSA) based on the paraelectric space group $P6_3/mmc$ have shown that the ferroelectric displacements in hexagonal manganites will only be favored along this axis [10]. In this ferroelectric phase there are six formula units ($YMnO_3$) per unit cell. The six Mn atoms occupy the z=0 and z=1/2 planes and are coordinated by oxygen atoms resulting in MnO_5 bipyramidal-type polyhedra [28]. In the z-zero plane Mn atoms occupy positions along the axes a_1, a_2, and $-(a_1 + a_2)$ and, in the z=1/2 plane along the axes $-a_1$, $-a_2$ and (a_1+a_2) [28]. This atomic arrangement leads to an $\sqrt{3} \times \sqrt{3}$ superstructure also known as trimerization of Mn atoms [29]. On the other hand, the six Y atoms are distributed among two symmetry inequivalent sites, in a ratio $2Y_1$ and $4Y_2$, that are displaced in an antiparallel manner (see Fig. 1) leading to a net polarization [1].

Based on the position of the atoms in the paraelectric $YMnO_3$ of $P6_3/mmc$ symmetry, the net displacements, dY, of all Y atoms from the centrosymmetric positions is zero, i.e. $2*dY_1=0$, and $4*dY_2=0$, so that $2*dY_1+4*dY_2 =0$. In the ferroelectric $P6_3cm$ phase the quantity $2*dY_1+4*dY_2$ (i.e. the total displacement of all yttrium atoms from their centrosymetric positions along the c-axis of the hexagonal unit cell) is not zero and so it may be used here as an effective local order parameter (OP). The values calculated for the OP using the Rietveld refined coordinates for Y atoms are shown in Fig. 5. Data in the Figure show that the net ferroelectricity-generating local displacements of Y atoms increase in absolute values with diminishing particles size.

The relative positioning of Y, Mn and O atoms is a very precise indicator of the ferroelectricity in $YMnO_3$. In this work we mostly concentrate on the Y atomic positions for two reasons. First, yttrium scatters strongly x-rays comparing to oxygen and manganese atoms and so the information content regarding Y atoms is abundant in the SXRD patterns and the atomic PDF extracted from them. Second, more importantly, as explained above Y atoms are at the structural origin of the ferroelectricity in $YMnO_3$. Positions of Y atoms can be very precisely computed from the structural models obtained by Rietveld analysis of the SXRD patterns. Those are, however, representative enough for the large size $YMnO_3$ particles only. To verify the results of the Rietveld analyzes for the larger size particles and obtain precise results for the smaller size ones we carried out atomic PDF analysis.

In Figure 6 the experimental atomic PDF's for $YMnO_3$ particles with sizes from 10 nm to 467 nm are shown. In the upper panel of the figure, PDF peaks reflecting the first neighbor distances corresponding to metal-oxygen, i.e. Mn-O and Y-O, and metal-metal, i.e. Y-Y and Mn-Mn, interatomic correlations are labeled, respectively. Note, due to the stronger x-ray scattering power of Y atoms, the Y-Y correlations are the major contributor to the PDF peaks reflecting the first neighbor metal-metal correlations. The PDF for bulk $YMnO_3$ exhibits well defined peaks to very high interatomic distances, characteristic of a material possessing a long-range, crystalline order. This experimental PDF data for $YMnO_3$ can be reproduced very well with the model refined by Rietveld analysis featuring a bulk ferroelectric phase (SG: $P6_3cm$). The excellent fit between the experimental and simulated PDF for 467 nm particles attests to the good quality of the high-energy SXRD experiments and atomic PDFs derivation. From the refined atomic positions in the $P6_3cm$-type structure model for 467 nm particles we calculated the ferroelectric polarization in $YMnO_3$ using the equation $P = \sum_i (dc_i Q_i em_i)/V$, where dc_i is the displacement of the atoms from the centrosymmetric position in Å, Q_i is the ionic charge, *e* is the electronic charge, m_i is the site multiplicity, and the unit cell volume is denoted by V. The polarization obtained by the Rietveld and PDF refined atomic coordinates is ~5.97 $\mu C/cm^2$. This value is very close to what is reported in the literature [30,31] for bulk $YMnO_3$. This result is a vivid demonstration of the power of diffraction

techniques to deliver structural parameters from which important material's properties can be estimated very precisely.

The experimental PDFs of the $YMnO_3$ particles smaller than 467 nm also show a series of well defined peaks. The peaks, however, become increasingly broader with diminishing particle size signaling increasing structural disorder. The disorder is strong and reduces the length of structural coherence to only a few nm with the smaller size particles. This length can be estimated from the real space distances where the experimental PDFs decay to zero. Note the structural coherence length estimated from the PDF data is substantially shorter than the average grain/particle's size. For 10 nm $YMnO_3$ particles this length is about 1 nm. A similar effect is seen in nanosized $BiFeO_3$, $BaTiO_3$, semiconductor quantum dots, and metallic nanoparticles [13-15, 32]. The increased structural disorder at the nanoscale appears to be a universal phenomenon and is often much stronger than the usual thermal disorder. This additional structural disorder manifests itself as an extra increase in the root-mean-square (rms) fluctuations of the atomic positions when the physical size of the system approaches nanoscale dimensions. These extra atomic rms fluctuations may interfere with the magnetic and ferroelectric orders in $YMnO_3$ and render them weaker as documented with the magnetic order for example [6]. Such disorder may not be described well within the crystallographic constraints of the hexagonal lattices based models used for bulk $YMnO_3$.

A careful analysis of the experimental PDFs of the smaller $YMnO_3$ particles shows that the effect of reduced particles size is somewhat similar to the "melting" of Bi-sublattice reported for $BiFeO_3$ [14]. The effect manifests itself in the fact that with the decrease in particles size the PDF peaks corresponding to Y-Y atomic pairs smear out more rapidly than those where other atoms (e.g. oxygen) are involved. In particular, the height of the peak corresponding to metal-metal first neighbor correlations diminishes drastically relative to the height of the peak reflecting the metal-oxygen correlations (follow the broken lines in Fig. 6). Indeed the latter change little with particles size. This observation suggests that metal-oxygen first coordination sphere is relatively intact while the first metal-metal coordination sphere suffers very substantial structural disorder. Since Mn atoms are tightly bound inside oxygen polyhedra and the Mn-atoms due magnetic ordering is found to survive in nanosized $YMnO_3$ [6] it is less likely that Mn

atoms themselves suffer a lot of local rms fluctuations. Apparently, those then may be associated with the Y atoms that occupy plenty of open space between the layers of Mn-O_5 polyhedra and so could move around yet retain its oxygen coordination (see the well-defined Y-O peak in the atomic PDFs of smaller size particles in Fig. 6). Our further PDFs analyses give strong evidence in support of this assumption.

In order to verify it at first we performed PDF fits using the constraints of the ferroelectric phase of $YMnO_3$ (SG: $P6_3cm$). We found that the fits worsen with diminishing particle size indicating that the $P6_3cm$ symmetry–based model should be modified (see Fig. 7(a, b) orange). This was done by releasing the Y atoms and allowing not only their z but also x and y coordinates to change. Thus modified model performed much better (see Fig. 7(a, b) wine red, and the substantially improved goodness-of-fit factors R_w) proving the feasibility of the assumption discussed above. Note the improvement is achieved by introducing minimal complexity in the underlying $P6_3cm$ structure model by only allowing the Y atoms to move within the plane between Mn-O_5 polyhedra. It is also important to note that during all PDF refinements (i.e. for all particle sizes) the thermal parameters were fixed to the values of 467 nm particles in order to avoid artificially enlarged thermal-type atomic displacements. The displacements of the 6 Y atoms from their centrosymmetric positions along x, y, and z directions derived from thus modified structure model are shown in Fig. 8. The results show increasing local displacements of Y atoms both in the xy plane and along the polar c-axis (i.e. z-direction) with diminishing particles size. The displacements of Y atoms along x, y, and z directions in nanosized $YMnO_3$ follows an exponential type functional dependence in line with predictions of analytical models [13a, 26, 27]. The variation of cell volume ($V_H=a_H^2c_H(\sqrt{3}/2)$), as obtained from these PDF refinements, is shown in Fig. 4b. It is similar to the findings of the Rietveld analysis. The nature of the order parameter OP obtained by the PDF fits, and its change with particle size, is also very similar to the predictions of the Rietveld analysis for larger size particles (see Fig. 5). Thus the two independent techniques show a similar trend, namely that the z-displacements of Y atoms and the ferroelectric local order parameter derived from them increases in absolute values with diminishing particles size. A similar phenomenon has been observed in nanosized

$BaTiO_3$ perovskite [13]. The x and y displacements of Y atoms, however, may interfere [1,12] with the locally increased ferroelectric order acting as extra planar disorder.

Previous studies on nanosized ferroelectric perovskites show that the extra structural disorder at the nanoscale gradually weakens the cooperative ferroelectricity to a point where it is greatly diminished becoming a hardly measurable bulk property [13,14]. In different ferroelectric materials this happens in a slightly different way as discussed below: In $BaTiO_3$ the bulk ferroelectricity is due to coupled tetragonal distortions of TiO_6 octahedra that are stabilized by the partial covalency of Ti *3d* – O *2p* orbitals. The tetragonal distortions increase locally with diminishing particles size [13a] but instead of being enhanced, the cooperative ferroelectricity gradually disappears since the extra rms atomic fluctuations in nanosized particles frustrates the long range ordering between the local (TiO_6)-based electric dipoles [13a]. On the other hand, in $BiFeO_3$ the $6s^2$ lone pair of Bi^{3+} hybridizes with O *2p* states resulting in a cooperative displacement of Bi sublattice with respect to the Fe-based oxygen octahedra and, hence, cooperative ferroelectricity arises. The extra rms atomic fluctuations in the nanoparticles, however, virtually melt the Bi-sublattice and so the cooperative ferroelectric order is expected to disappear [14]. Thus different ABO_3 ferroelectric materials respond differently to the extra structural disorder at the nanoscale. Bismuth atoms in $BiFeO_3$ are somewhat small to fit tightly into the dodecahedra of the perovskite structure and, hence, are quite susceptible to local structural disorder. By contrast, Ba atoms in $BaTiO_3$ are big enough to fit tightly into the dodecahedra and so remain coupled to the structurally coherent lattice of TiO_6 octahedra even when subjected to increased rms fluctuation at the nanoscale. Although layered, and not a three-dimensional network like $BaTiO_3$ and $BiFeO_3$, hexagonal $YMnO_3$ is similar to both perovskites discussed above. Yttrium atoms in $YMnO_3$ have relatively small ionic radius, and occupy fairly open space between layers of MnO_5 polyhedra. Thus the extra structural disorder at the nanoscale affects mostly the Y atoms in $YMnO_3$ just like it affects mostly the Bi atoms in nanosized $BiFeO_3$ [14]. On one hand, this disorder brings in enhanced (in absolute values) displacements of Y atoms along the polar c axis, i.e. an enhancement of the local structural origin of the ferroelectricity, similarly to the increase in the local Ti-O displacements in $BaTiO_3$ [13a,b]. On the other hand, the extra x,y-planar disorder of the

Y atoms may interfere with the cooperative ferroelectricity of nanosized $YMnO_3$. Evidently future efforts to employ $YMnO_3$ in nanoscale applications should take them into account.

4. Conclusions

In summary, high-energy synchrotron XRD and atomic PDFs studies reveal that reducing $YMnO_3$ to nanosized dimensions results in i) an increased x,y-planar disorder of the Y atoms and ii) an increase of the polar displacements of Y atoms along the c axis of the hexagonal unit cell. At the same time the Mn-O network is much less disturbed structurally. This picture is somewhat similar to what is observed in nanosized $BiFeO_3$ and $BaTiO_3$. The new knowledge about the atomic-scale structure of freestanding $YMnO_3$ nanoparticles can provide much needed basis for their exploration in technology applications.

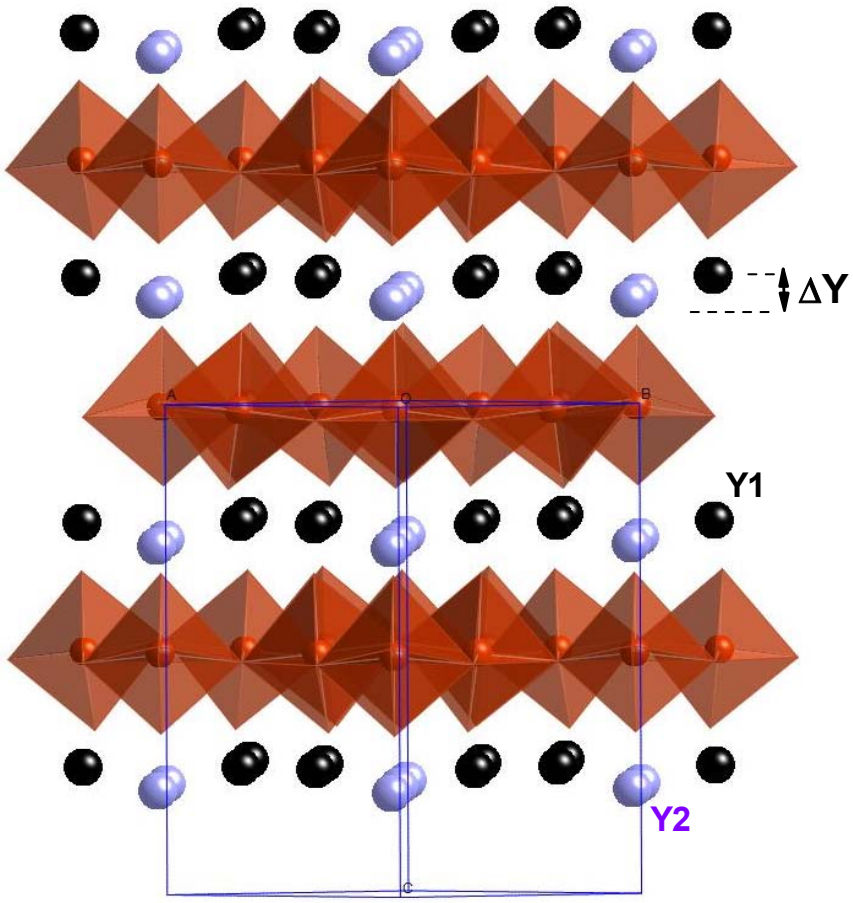

Figure 1: (color on-line) Fragment from the room temperature hexagonal structure of $YMnO_3$ featuring layers of MnO_5 polyhedra (brown) and two types of Y atoms (black and magenta) in between. Note the displacement of two types of Y atoms, $\Delta Y \neq 0$, with respect to each other in this ferroelectric $YMnO_3$ phase. In the high-temperature paraelectric phase Y atoms occupy centrosymmetric positions and $\Delta Y = 0$.

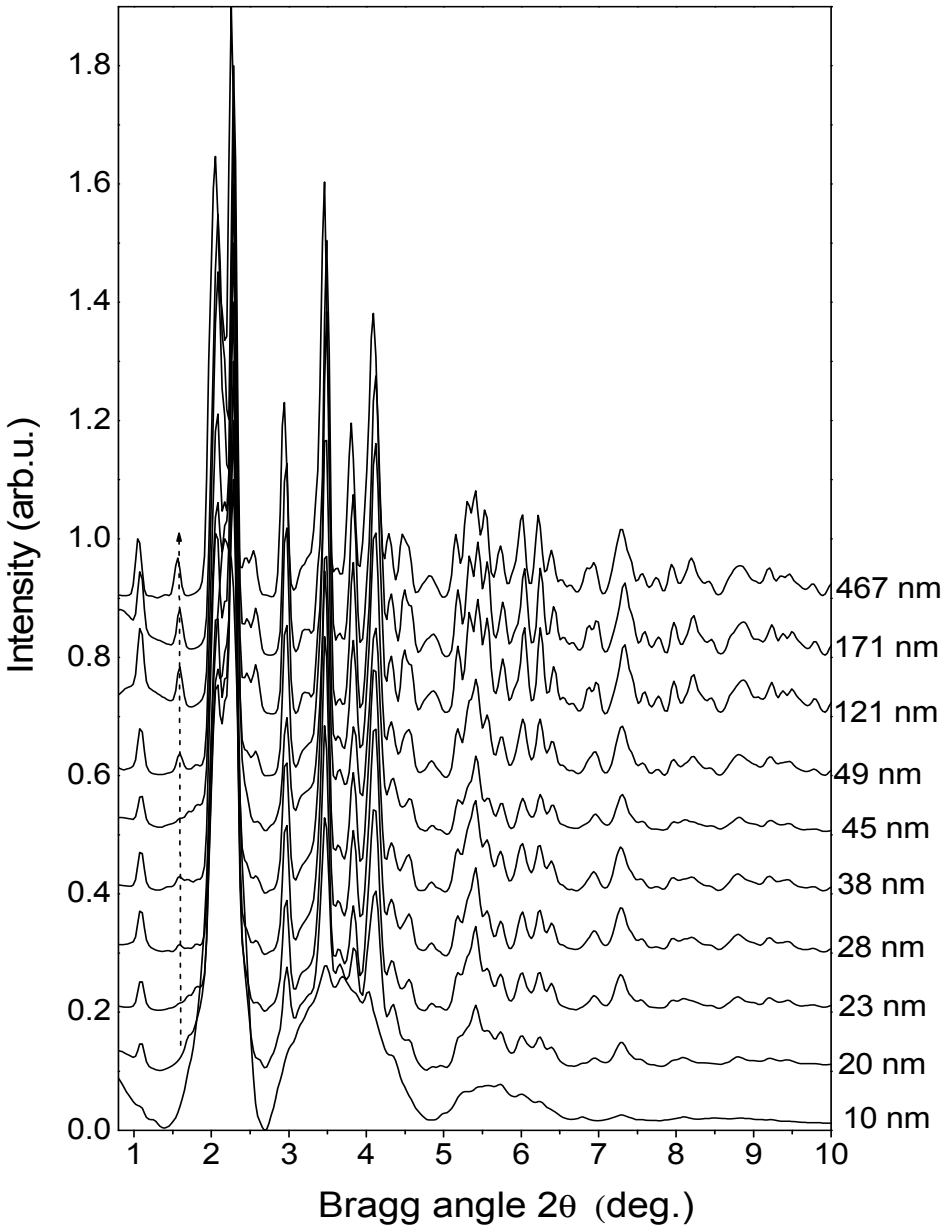

Figure 2: SXRD patterns of $YMnO_3$ for particles with size ranging from 467±42 nm to 10±1 nm. For clarity only a relatively low-angle portion of the XRD patterns is shown. Sharp Bragg peaks are seen in the XRD patterns for the larger size particles. The peaks broaden and merge into an intensive diffuse component with diminishing particle size. Dotted line marks the so-called superlattice peaks as explained in the text.

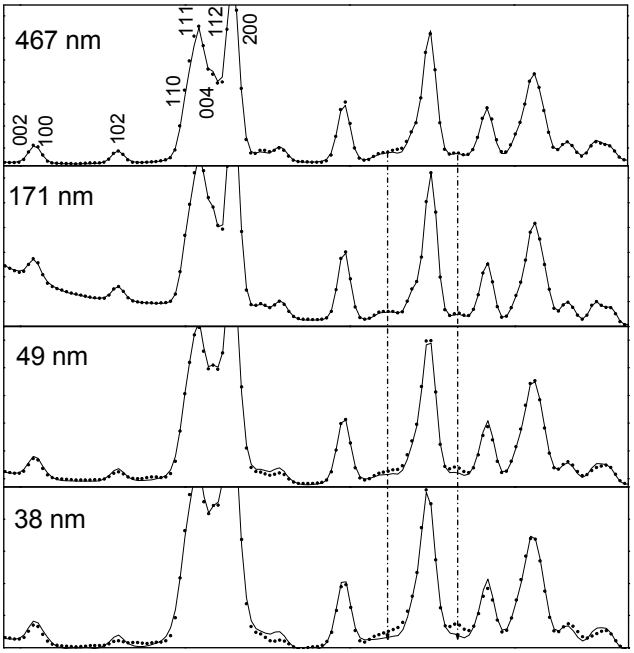

Figure 3: Observed (dots) and Rietveld fit (continuous line) SXRD patterns of $YMnO_3$ particles of selected sizes. The fits were done employing a hexagonal structure model (S.G. $P6_3cm$). The quality of the fits worsens (follow the broken arrow lines) with diminishing particles size. Selected peaks are marked with the respective Miller (hkl) indices.

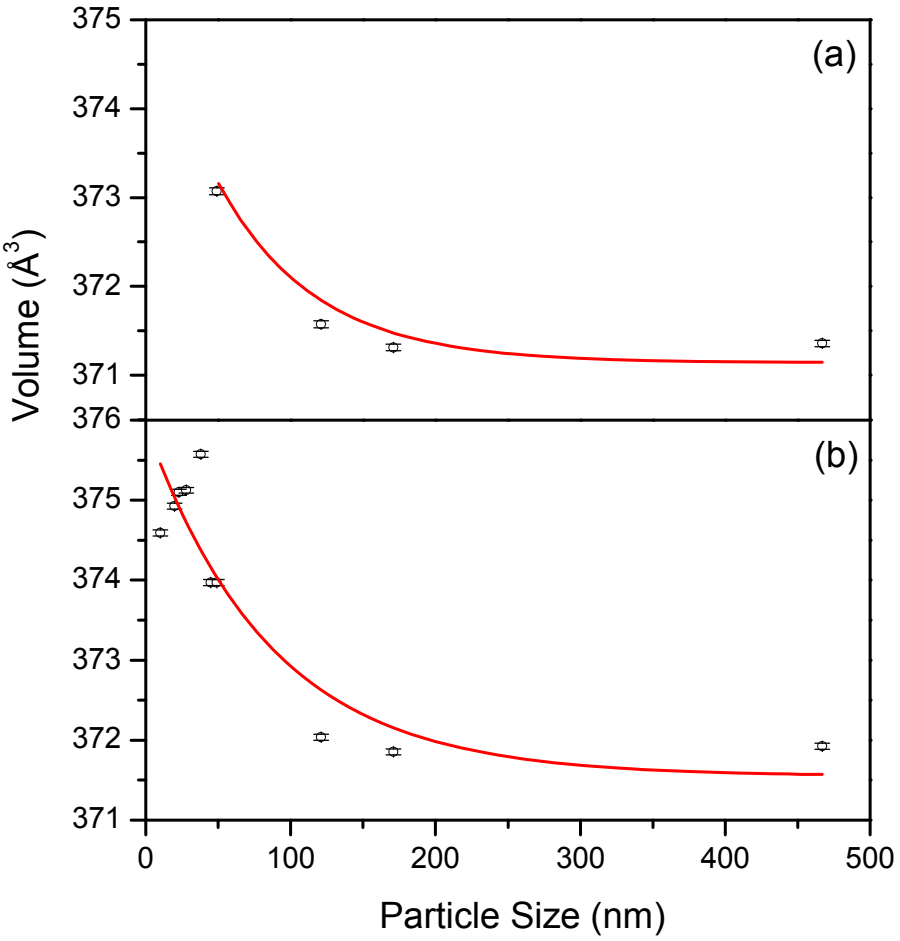

Figure 4: (color on line) Evolution of the hexagonal unit cell volume with particles size of $YMnO_3$ as obtained from (a) Rietveld fits to the SXRD patterns and (b) PDF fits of Fig.7 (b). An exponential increase (red line) in the unit cell volume with diminishing particles size is observed. Note $YMnO_3$ particles of a larger (> 38 nm) size are crystalline in nature and so are very well approximated by a model featuring a periodic lattice of hexagonal ($P6_3cm$) symmetry. The unit cell of this lattice is a very well defined quantity. The particles of smaller (< 38 nm) size are less crystalline in nature yet fairly well approximated by a model based on the same hexagonal lattice where only Y atoms have been released from the symmetry constraints of S.G. $P6_3cm$. The unit cell of thus modified lattice remains a well defined quantity that may be directly compared to the unit cell of the unmodified lattice.

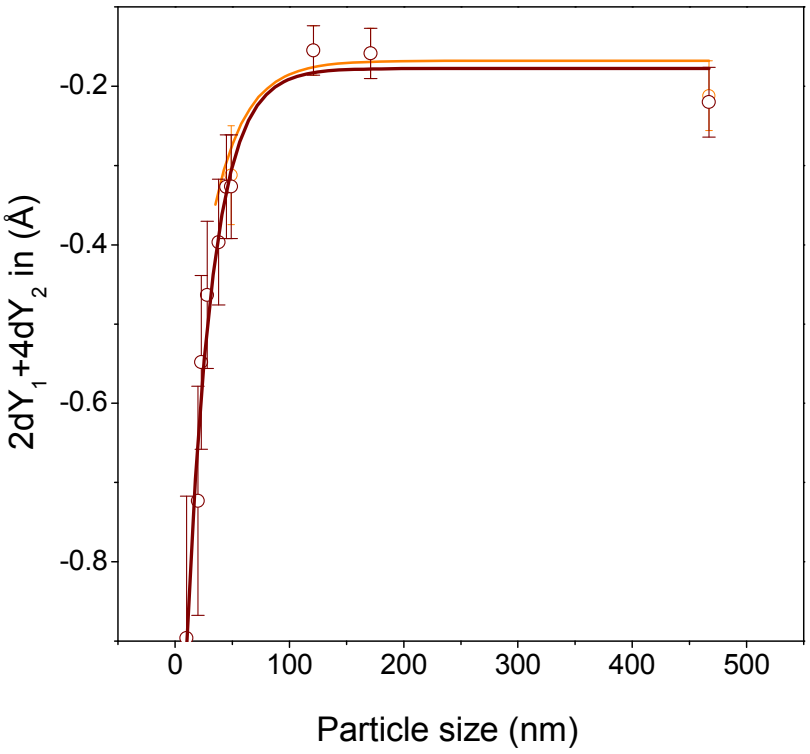

Figure 5: (color on line) Evolution of the ferroelectricity "local order parameter" OP=2*d_z(Y1)+4*d_z(Y2) with particle size derived from Rietveld (line in orange) and PDF analyzes (line in wine red). An exponential fit approximates the evolution quite well. The parameter is seen to increase in absolute value with diminishing particles size.

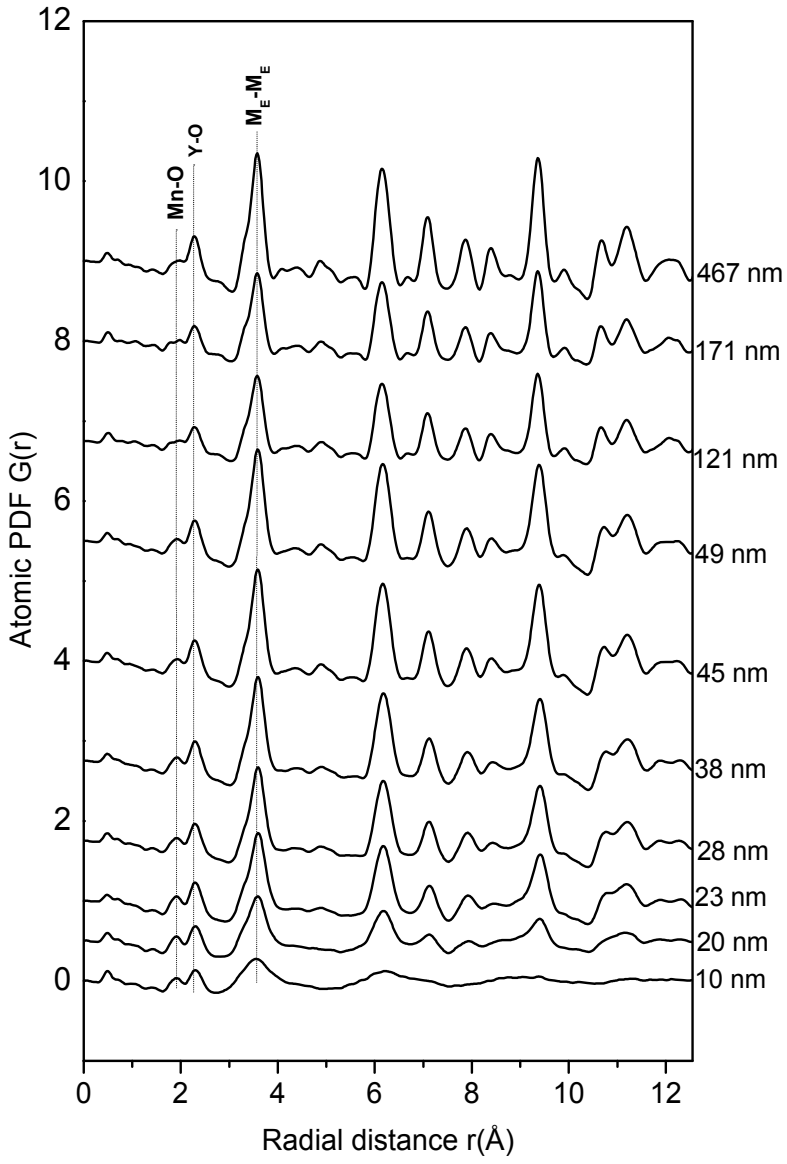

Figure 6 : Low-r part of the experimental atomic PDFs G(r) for $YMnO_3$ particles. The PDF peaks are well defined with the larger size particles reflecting the high degree of crystallinity in those samples. The PDF peaks progressively broaden with diminishing particles size indicating an increased degree of structural disorder at the nanoscale. Peaks corresponding to first metal-oxygen and metal-metal (M_E=Y, Mn) correlations are labeled with the respective atomic pairs.

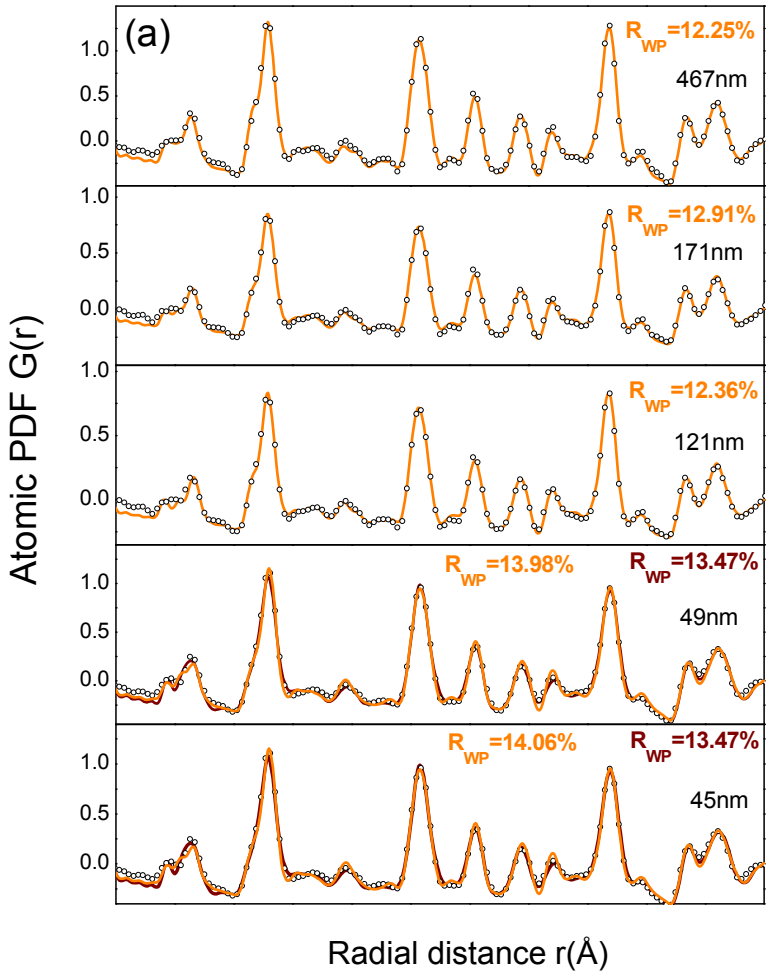
(a)
R_WP=12.25%
467nm
R_WP=12.91%
171nm
R_WP=12.36%
121nm
R_WP=13.98%
R_WP=13.47%
49nm
R_WP=14.06%
R_WP=13.47%
45nm
1.0
0.5
0.0
Atomic PDF G(r)
Radial distance r(Å)

Figure 7a:

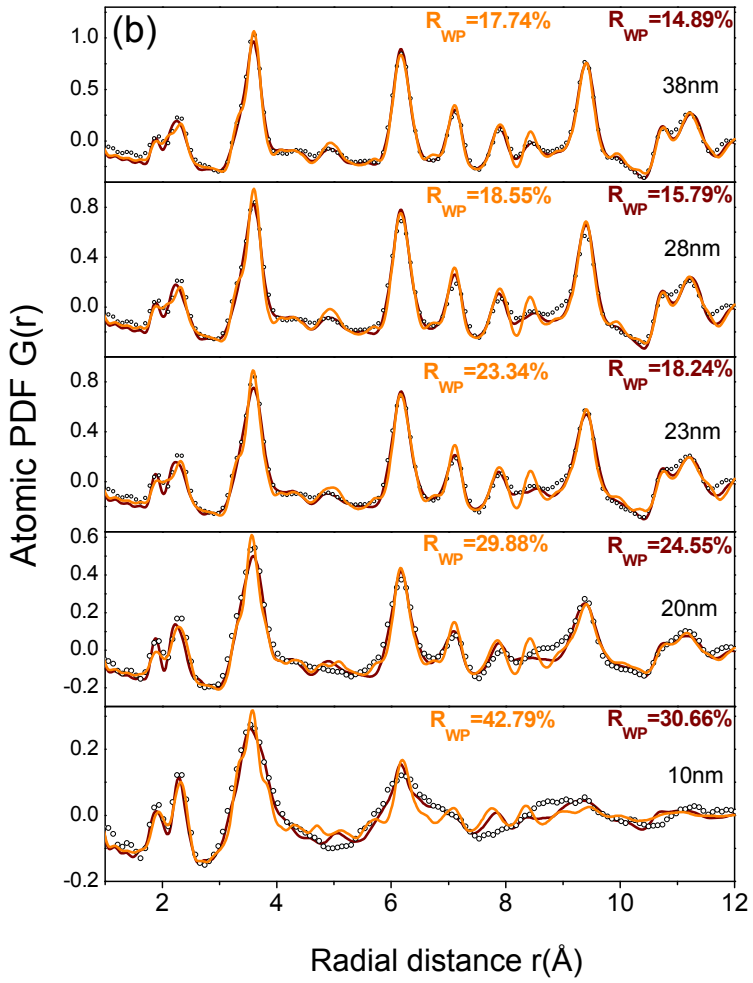

Figure 7b:

Figure 7: (color on line) (a) Experimental (symbol), model 1 (line in orange) and model 2 (line in wine red) PDFs for $YMnO_3$ particles of sizes from 45 to 467 nm. Data in the range of 1-12 Å are only shown for the sake of clarity. The model 1 data are computed strictly observing the constraints of a hexagonal lattice of $P6_3cm$ symmetry. The model 2 data are also computed on the basis of a hexagonal structure (S.G. $P6_3cm$) where Y atoms have been allowed to move within a plane between Mn-O_5 polyhedra. Note in (a) this breaking of the local Y atoms symmetry hardly affects the quality of the PDF fits indicating very limited, if any, planar disorder of Y atoms. With the smaller size particles (b) the breaking of the local Y atoms symmetry substantially improves the fits to the atomic PDFs especially in the range of *r* values from 2 to about 10 Å. No attempts to improve the fits further were made since in this work we concentrate on the Y atoms relative positioning that is at the structural origin of the ferroelectricity in $YMnO_3$.

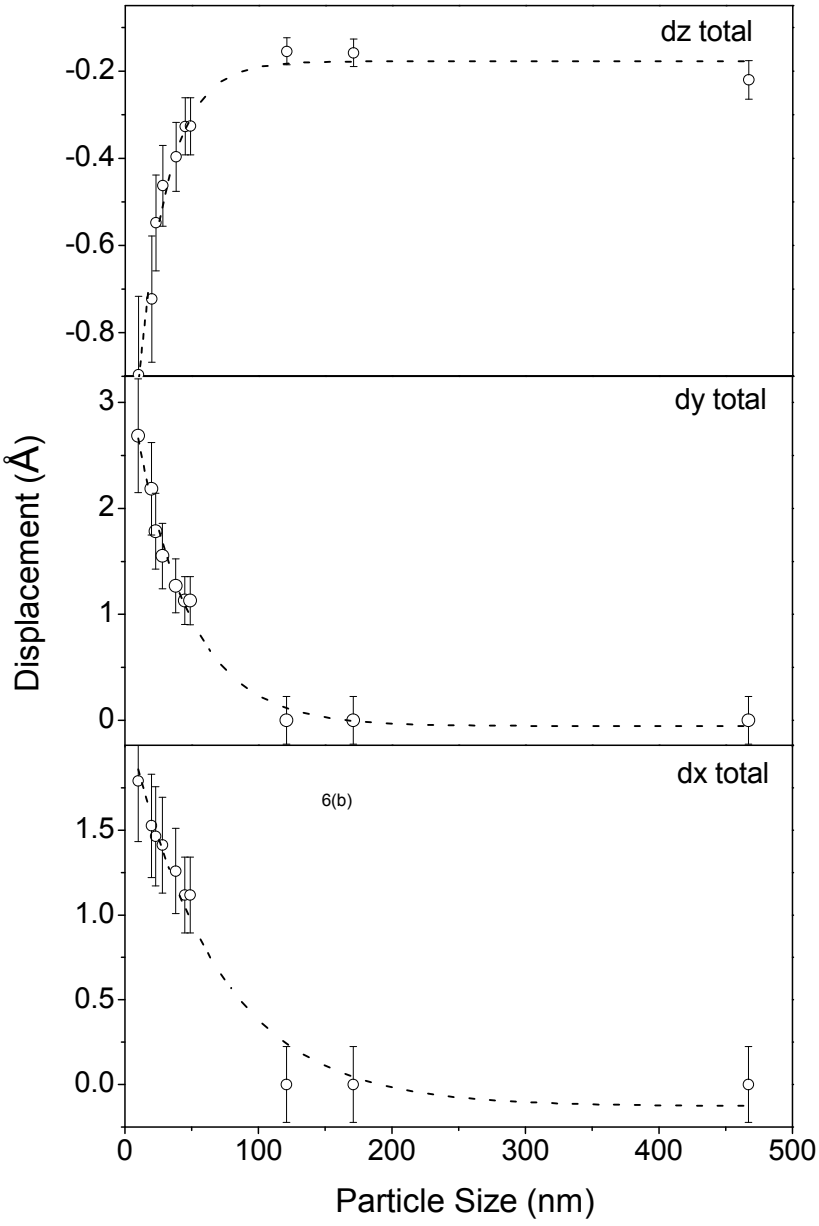

Figure 8: Variation of Y atoms displacements along x, y and z directions as determined by atomic PDFs analysis. The displacements along the x and y directions feature planar disorder, whereas along the z direction contribute to the local ferroelectric order. The dashed line fits show an exponentially increasing (in absolute values) both planar (x,y) disorder and contribution (z-displacement) to the ferroelectricity in $YMnO_3$ with diminishing particles size.

Acknowledgements: Work at APS is supported by DOE under Contract DEAC02-06CH11357. Partial support from DOE-BES via Grant DE-SC0006877 and from the strategic area MATERIALS at NTNU is also acknowledged.

References:

1. B. B. Van Aken, T. T. M. Palstra, A Filippetti and N A Spaldin, Nat. Mater. **3**, 164 (2004).
2. M. Fiebig, T. Lottermoser, D. Frohlich, A. V. Goltsev and R. V. Pisarev, Nature **419**, 818 (2002); R. Ramesh and N. A. Spaldin, Nature Mater. **6**, 21 (2007); M. Feibig, J. Appl. D: Appl Phys **38**, R123 (2005).
3. S.W. Cheong and M. Mostovoy, Nature Mater. **6**, 13 (2007); W. Eerenstein, N. D. Mathur, and J. F. Scott, Nature (London) **442**, 759 (2006).
4. I. G. Ismailzade and S. A. Kizhaev, Sov. Phys. Solid State **7**, 236 (1965).
5. D. G. Tomuta, S. Ramakrishnan, G. J. Nieuwenhuys, and J. A. Mydosh, J. Phys.: Condens. Matter **13**, 4543 (2001).
6. Tai- Chun Han, Wei-Lun Hsu, Wei-Da Lee, Nanoscale Res. Lett. **6**, 201 (2011).
7. H. L. Yakel, W. C. Koehler, E. F. Bertaut, and E. F. Forrat, Acta Crytallogr, **16**, 957, (1963).
8. A. S. Gibbs, K. S. Knight, and P. Lightfoot, Phys. Rev. B **83**, 094111 (2011).
9. N. A. Hill, J. Phys. Chem. B **104**, 6694 (2000).
10. A. Filippetti and N. A. Hill, Phys. Rev. B **65**, 195120 (2002).
11. (a) D.-Y. Cho, J. –Y. Kim, B. –G. Park, K. –J. Rho, J. –H. Park, H.-J. Noh, B. J. Kim, S.-J. Oh, H.-M. Park, J. –S. Ahn, H. Ishibashi, S-W. Cheong, J. H. Lee, P. Murugavel, T. W. Noh, A. Tanaka, and T. Jo, Phys. Rev. Lett. **98**, 217601, (2007);
    (b) J. Kim, K. C. Cho, Y. M. Koo, K. P. Hong, and N. Shin, Appl. Phys. Lett. **95,** 132901 (2009).
12. Y. Kumagai, A. A. Belik, M. Lilienblum, N. Leo, M. Fiebig, and N. A. Spaldin, Phys. Rev. B **85**,174422 (2012).
13. (a) V. Petkov, V. Buscaglia, M. T. Buscaglia, Z. Zhao and Y. Ren, Phys Rev. B **78**, 054107 (2008); (b) K. Page, T. Proffen, M. Niederberger, and R. Seshadri. Chem. Mater. **22**, 4386 (2010); (c) M. J. Polking, M.-G. Han, A. Yourdkhani, V. Petkov, C.

F. Kisielowski, V. V. Volkov, Y. Zhu, G. Caruntu, A. P.Alivisatos and R. Ramesh Nat. Mat. 3371 (2012), published on-line.

14. V. Petkov, S. M. Selbach, M.-A. Einarsrud, T. Grande and S. D. Shastri, Phys Rev. Lett **105**, 185501 (2010).
15. V. Petkov, N. Bedford, M. R. Knecht , M. G. Weir , R. M. Crooks , W. Tang , G. Henkelman and A. Frenkel, J. Phys. Chem. C 112, 8907 (2008).
16. I. I. Naumov, L. Bellaiche, and H. Fu, Nature (London) **432**, 737 (2004).
17. M. D. Hughes, Yi-J. Xu, P. Jenkins, P. McMorn, P. Landon, D. I. Enache, A. F. Carley, G. A. Attard, G. J. Hutchings, F. King, E. H. Stitt, P. Johnston, K. Griffin and C. J. Kiely, Nature (London) **437**, 1132 (2005).
18. W. L. Zhong, Y. G. Wang, P. L. Zhang, and B. D. Qu, Phys. Rev. B **50**, 698 (1994).
19. S. Li, J. A. Eastman, Z. Li, C. M. Foster, R. E. Newham, and L. E. Cross, Phys. Lett. A **212**, 341(1996).
20. S. Lin, T. Lu, Ch. Jin, and X. Wang, Phys. Rev. B **74**, 134115 (2006).
21. T. Egami, and S. J. L. Billinge, Underneath the Bragg peaks (Pergamon Press, Amsterdam, 2003).
22. K. Bergum, H. Okamoto, H. Fjellvåg, T. Grande, M.-A. Einarsrud and S. M. Selbach, Dalton Trans. **40** 7583 (2011).
23. K. Kamata, T. Nakajima and T. Nakamura, Mater. Res. Bull. 14, 1007 (1979)
24. J. Rodríguez-Carvajal, Physica B **192**, 55 (1993).
25. C.L. Farrow, P Juhás, J.W Liu, D. Bryndin, E. Božin, S. J. Bloch, Th. Proffen, and S.J.L. Billinge, *J. Phys.: Condens. Matter* **19***,* 335219-7 (2007).
26. G. Guisbiers, Nanoscale Res Letters **5**, 1132 (2010).
27. C. Yang, Z. F. Zhou, J. W. Li, X. X. Yang, W. Qin, R, Jiang, N. G. Guo, Y. Yang and C. Q. Sun, Nanoscale **4,** 1304(2012).
28. A. Munoz, J. A. Alonso, M. J. Martinez-Lope, M. T. Casais, J. L. Martinez, and M. T. Fernandez-Diaz, Phys. Rev. B **62**, 9498 (2002).
29. T. Katsufuji, M. Masaki, A. Machida, M. Moritomo, K. Kato, E. Nishibori, M. Takata, M. Sakata, K. Ohoyama, K. Kitazawa, and H. Takagi, Phys. Rev. B **66**, 134434 (2002).

30. B. B. Van Aken, A. Meetsma, T. T. M. Palstra, Acta. Cryst. C **57**, 230 (2001); B. B. Van Aken, A. Meetsma, T. T. M. Palstra, Acta. Cryst. E **57**, i**38** (2001); ibid. i**87**, ibid. i101; N. Fujimara, T. Ishida, T. Yoshimura, and T. Ito, Appl. Phys. Lett. **69**, 1011 (1996).

31. S.M. Selbach, T. Tybell, M-A. Einarsrud and T. Grande, Chem. Mat. **19,** 6479 (2007).

32. (a) B. Gilbert, F. Huang, H. Zhang, G. A. Waychunas, J. F. Banfield, Science **305**, 651 (2004); (b) V. Petkov, I. Moreels, Z. Hens, and Y. Ren, Phys. Rev. B **66**, 241304(R) (2010).